

# **Numerical Simulation of Forced and Free-to-Roll Delta-Wing Motions**

Neal M. Chaderjian and Lewis B. Schiff

Reprinted from

## **Journal of Aircraft**

Volume 33, Number 1, Pages 93-99



*A publication of the*  
American Institute of Aeronautics and Astronautics, Inc.  
370 L'Enfant Promenade, SW  
Washington, DC 20024-2518

# Numerical Simulation of Forced and Free-to-Roll Delta-Wing Motions

Neal M. Chaderjian\* and Lewis B. Schiff†  
NASA Ames Research Center, Moffett Field, California 94035

The three-dimensional, Reynolds-averaged, Navier–Stokes (RANS) equations are used to numerically simulate nonsteady vortical flow about a 65-deg sweep delta wing at 30-deg angle of attack. Two large-amplitude, high-rate, forced-roll motions, and a damped free-to-roll motion are presented. The free-to-roll motion is computed by coupling the time-dependent RANS equations to the flight dynamic equation of motion. The computed results are in good agreement with the forces, moments, and roll-angle time histories. Vortex breakdown is present in each case. Significant time lags in the vortex breakdown motions relative to the body motions strongly influence the dynamic forces and moments.

## Introduction

THE high angle-of-attack flight regime often includes complex phenomena such as nonsteady flow, crossflow separation, and vortex breakdown. Modern tactical fighters fly at high angles of attack in order to take advantage of the nonlinear lift generated from vortices that form on their leeward sides. This results in a substantial improvement of an aircraft's maneuver and agility performance. However, at sufficiently high angles of attack, vortex asymmetries can form and induce dynamic motions such as wing rock, a sustained limit-cycle roll and yaw oscillation. Wing rock and other self-induced aircraft motions can be difficult to control and may result in departure from controlled flight.

A number of experiments<sup>1–12</sup> have investigated wing rock and other dynamic motions for delta-wing geometries with a single-degree-of-freedom in roll. These simple geometries contain the relevant flow physics, e.g., primary, secondary, and tertiary vortices, and vortex breakdown, without the additional complexities of a complete aircraft geometry. Experimental data usually include forces and moments, as well as on-surface and off-surface flow visualization. More recently, some experiments<sup>6–12</sup> have also measured time-dependent surface pressures.

Computational fluid dynamics (CFD) is just beginning to be used to investigate wing rock. CFD can provide greater flowfield detail than is otherwise possible by experiment alone, and therefore, complements experimental investigations. However, CFD flow simulations can be computationally costly because the flowfield is often nonsteady and highly nonlinear. Some investigators have reduced the computational cost by employing the inviscid Euler equations in conical<sup>13–15</sup> or three-dimensional<sup>16</sup> form. Although these simplifications reduce the computational cost, they inherently eliminate prediction of a number of relevant flow features. For example, in the conical assumption, similarity principles are used to reduce a three-

dimensional physical flow into a two-dimensional computation. As a result, this approach cannot predict vortex breakdown that often accompanies wing rock. Furthermore, methods based on the assumption of inviscid flow only predict vortex formation emanating from flow separation at sharp leading edges. The inviscid assumption completely ignores the vortices that are known to form from separation at smooth surfaces, e.g., forebody, secondary, and tertiary vortices. The strength of the inviscid primary vortices is also questionable and may affect the position of vortex breakdown. Ultimately, these computational simplifications will have only restricted utility for complete aircraft applications.

The approach adopted in this work is to utilize the Navier–Stokes simulation (NSS) code to numerically compute high-incidence vortical flow about a delta wing by solving the time-dependent, three-dimensional, Reynolds-averaged, Navier–Stokes (RANS) equations. Although this approach is more computationally costly, it contains all of the relevant flow physics. It is also anticipated that future computer improvements will continue to reduce the computer time needed to obtain time-dependent RANS solutions.

The overall goal of this effort is to develop an experimentally validated CFD tool for predicting and analyzing static roll, forced dynamic-roll motions, and free-to-roll motions for delta wings at high incidence using the RANS equations. Chaderjian<sup>17</sup> previously used the NSS code to predict the vortical flow over a 65-deg sweep delta wing at 0.27 Mach number and 15-deg angle of attack. The computed static and dynamic forces and moments, and time-dependent surface pressures were in very good agreement with large-amplitude, high-rate-motion experiments.<sup>10</sup> The rolling moment coefficient  $C_l$  comparisons are shown in Fig. 1. The roll angle  $\phi$

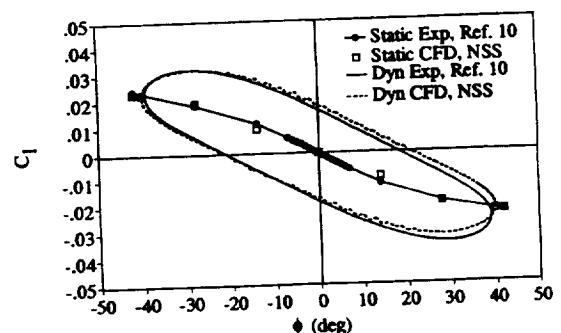


Fig. 1 Static and dynamic rolling-moment coefficients from Ref. 17.  $M_\infty = 0.27$ ,  $\alpha = 15$  deg,  $Re = 3.67 \times 10^6$ , and  $k = 0.14$  for the dynamic case.

Presented as Paper 94-1884 at the AIAA 12th Applied Aerodynamics Conference, Colorado Springs, CO, June 20–23, 1994; received Oct. 2, 1994; revision received Aug. 1, 1995; accepted for publication Aug. 2, 1995. Copyright © 1995 by the American Institute of Aeronautics and Astronautics, Inc. No copyright is asserted in the United States under Title 17, U.S. Code. The U.S. Government has a royalty-free license to exercise all rights under the copyright claimed herein for Governmental purposes. All other rights are reserved by the copyright owner.

\*Research Scientist, Applied Computational Aerodynamics Branch, Associate Fellow AIAA.

†Research Scientist, Aeronautical Technologies Division, Associate Fellow AIAA.

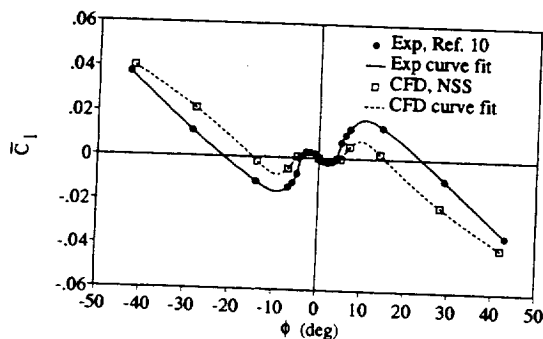


Fig. 2 Comparison of mean computed and experimental rolling-moment coefficients for different static roll angles from Ref. 18.  $M_\infty = 0.27$ ,  $\alpha = 30$  deg,  $Re = 3.67 \times 10^6$ .

corresponds to an angular rotation about the wing's longitudinal axis. Note the very good agreement for static  $C_l$  up through 42-deg of roll. The negative slope indicates this wing is statically stable in roll under the present flow conditions and has a trim point at  $\phi = 0$  deg. Also shown in the figure is a comparison of computed and experimental  $C_l$  for a large amplitude ( $\phi_{\max} = 40$  deg), high-rate (7-Hz), forced-roll motion. Hysteresis in the dynamic  $C_l$  vs  $\phi$  curve is due to roll rate effects. The dynamic  $C_l$  traces out the curve in a counterclockwise direction with increasing time, indicating that this wing is positively damped in roll. The areas enclosed by the dynamic curves, indicative of the aerodynamic damping coefficient, matched within 3%. At this angle of attack no vortex breakdown was observed in either the computed or experimental flows.

Chaderjian and Schiff<sup>18</sup> later computed the flowfield about the same 65-deg sweep delta wing at 30-deg angle of attack and several fixed roll angles, where vortex breakdown does occur. The mean static rolling-moment coefficient variation with roll angle is shown in Fig. 2. Note the nonlinear behavior of  $C_l$  for small roll angles. This was attributed to vortex breakdown. Three statically stable trim points and two statically unstable trim points are observed in both the computed and experimental results. The overall agreement is good, but some differences are apparent. It is anticipated that grid refinement will improve the comparison. Nevertheless, the present grid (about 700,000 grid points), was sufficient to predict the rolling-moment nonlinearity.

The purpose of this article is to build upon the previous two results by computing the flowfield for dynamic-roll motions of the 65-deg sweep delta wing at 30-deg angle of attack, where vortex breakdown does occur. Two forced-roll oscillations and a damped free-to-roll motion are presented. The free-to-roll results are obtained by coupling the RANS equations to the flight dynamic equation of motion with a single-degree-of-freedom in roll.

A summary of the wind-tunnel experiment used to validate the computations is given later. This is followed by a description of the numerical approach, which includes the governing equations, turbulence model, numerical algorithm, computational grids, and numerical boundary conditions. Computational results are then presented and followed by concluding remarks.

### Summary of Wind-Tunnel Experiment

Extensive wind-tunnel investigations for a 65-deg leading-edge sweep delta wing at high incidence were carried out by Hanff and his colleagues<sup>6-11</sup> in the Canadian Institute for Aerospace Research  $6 \times 9$  ft Low Speed Wind Tunnel and in the Wright Laboratory  $7 \times 10$  ft Subsonic Aerodynamic Research Laboratory (SARL) tunnel. Very high-quality experimental data was obtained for static (fixed) roll, forced dynamic-roll motions, and free-to-roll motions in the form of mean and time-dependent surface pressures, forces, and mo-

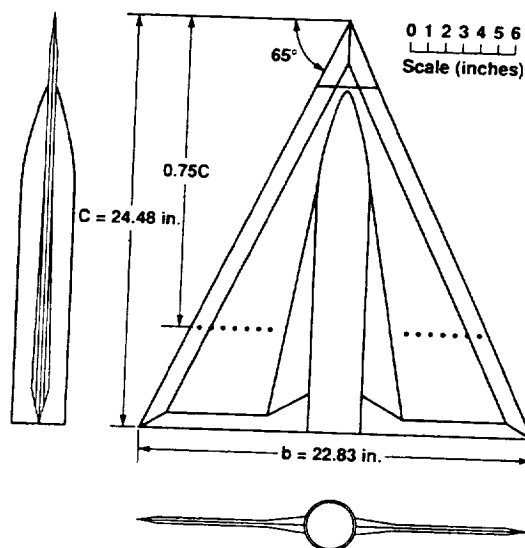


Fig. 3 Three-view drawing of the wind-tunnel model.

ments. A laser light sheet technique was used to visualize nonsteady off-body vortices, whereas an oil flow technique was used to visualize surface-flow patterns for static roll cases. These experimental data<sup>10</sup> are used to validate the present flow computations.

A three-view drawing of the delta-wing model is shown in Fig. 3. The delta wing is symmetric relative to its longitudinal axis and has double bevels that run parallel to and along the wing's leading and trailing edges. The delta wing is mounted on a fuselage/sting that contains instrumentation and allows for a single degree of freedom in roll. The fuselage has a tangent-ogive cylinder shape and the sting has a reduced diameter aft of the wing trailing edge. Bevels join the fuselage to the flat wing surface for additional stiffness. The model is constructed of a multilayer carbon-composite skin and foam core, resulting in a stiff, lightweight model having a low rolling moment of inertia. Dynamic pressure transducers are located across the span of the wing on the upper surface at 75% of the root chord. Further details about the experiment can be found in Refs. 6-9.

### Numerical Approach

#### Governing Equations

The time-dependent RANS equations are transformed from Cartesian coordinates ( $x, y, z$ , and  $t$ ) to body-fitted curvilinear coordinates ( $\xi, \eta, \zeta$ , and  $\tau$ ) to simplify the implementation of boundary conditions. The thin-layer approximation is used, where it is assumed that viscous terms are most significant in the body-normal  $\zeta$ -coordinate direction. This approximation is consistent with the high Reynolds number flow conditions presented next. The RANS equations can therefore be expressed in the following strong conservation-law form:

$$\partial_t \hat{Q} + \partial_\xi \hat{E} + \partial_\eta \hat{F} + \partial_\zeta \hat{G} = Re^{-1} \partial_\zeta \hat{S} \quad (1)$$

where  $\hat{Q}$  is the vector of conserved dependent variables,  $\hat{E}$ ,  $\hat{F}$ , and  $\hat{G}$  are the inviscid flux vectors in the  $\xi$ ,  $\eta$ , and  $\zeta$  directions, respectively, and  $\hat{S}$  is the thin-layer viscous flux vector. These equations have been nondimensionalized by the wing root chord  $C$ , the freestream density  $\rho_\infty$ , and the freestream speed of sound  $a_\infty$ . Any body movement or grid deformation is accommodated through coordinate transformation metrics that are included in the flux vectors. The perfect gas law, Sutherland's viscosity law, and a turbulence model completes the RANS system of equations. A description of the turbulence model is given in the next section. Further details of Eq. (1) can be found in Ref. 19.

The NSS code currently has the capability to compute flows about a delta wing with a single degree of freedom in roll about its longitudinal axis. The roll angle for a forced periodic motion is given by

$$\phi(t) = \Phi_0 + \Phi_{\max} \cos(\omega t) \quad (2)$$

where  $\Phi_0$  is the mean or offset roll angle,  $\Phi_{\max}$  is the amplitude of motion,  $\omega$  is the circular frequency ( $\omega = 2\pi f$ ), and  $t$  is the time variable. The reduced frequency is defined by

$$k = \omega b / 2V_\infty \quad (3)$$

where  $b$  is the span of the delta wing and  $V_\infty$  is the freestream speed. The roll angle for a free-to-roll motion, where the aerodynamics and body motion are coupled, is given by

$$I\ddot{\phi} + C_1 \text{sgn}(\dot{\phi}) = l(t) \quad (4)$$

where  $I$  is the rolling moment of inertia,  $\dot{\phi} = d\phi/dt$  and  $\ddot{\phi} = d^2\phi/dt^2$  are the angular velocity and acceleration, respectively, and  $l(t)$  is the instantaneous rolling moment obtained from the coupled time-dependent RANS equations. The second term on the left-hand side is a model for the mechanical bearing friction, where

$$\text{sgn}(\dot{\phi}) = \begin{cases} 1, & \dot{\phi} > 0 \\ 0, & \dot{\phi} = 0 \\ -1, & \dot{\phi} < 0 \end{cases}$$

Hanff<sup>10</sup> reported that  $I = 0.27 \text{ lb-in.} \cdot \text{s}^2$  and  $C_1 = 4.0 \text{ lb-in.}$  So the bearing friction of the experimental roll mechanism can be modeled as a small constant. Equations (2) and (4) define the roll angle for rigid body and grid motions.

#### Turbulence Model

The Baldwin-Lomax algebraic model<sup>20</sup> together with the Degani-Schiff modification<sup>21,22</sup> are used to model turbulent flow conditions. This is an efficient isotropic eddy-viscosity model that properly accounts for crossflow separation in the presence of strong vortices above the wing. The original unmodified Baldwin-Lomax model often chooses a length scale associated with a vortical flow structure that lies outside the viscous boundary layer. This results in an eddy viscosity that can be one or two orders of magnitude too large, and effectively suppresses all but the most dominant vortex structure. The modified model of Degani and Schiff restricts the choice of length scale to the boundary-layer region in a rational manner, and therefore, gives appropriate values for the eddy viscosity.

Experimental surface-flow patterns<sup>10</sup> indicate that the Reynolds number based on the wing root chord ( $Re_c = 3.67 \times 10^6$ ) is sufficiently high that turbulent transition is confined to a very small region near the delta-wing apex. The computations therefore assume fully turbulent flow beginning at the apex of the delta wing, i.e., transitional effects are ignored.

#### Numerical Algorithm

There is a choice of two implicit, approximately factored, central difference algorithms in the NSS code to integrate Eq. (1). The choice of algorithm is case dependent. The first algorithm is the Beam-Warming algorithm<sup>23</sup> and the second is a diagonal version of the Beam-Warming algorithm due to Pulliam and Chaussee.<sup>24</sup> Both algorithms, as currently implemented in the NSS code, use Euler implicit time differencing with first-order time accuracy and treat the viscous terms in an explicit manner. Both algorithms use second-order-accurate central differencing throughout, with added artificial dissipation to damp out high-frequency errors. The dissipation is automatically reduced within a boundary layer by scaling the dissipation terms with the square of the local fluid speed.<sup>25</sup> A cutoff switch prevents the dissipation from getting too small

near solid surfaces. Explicit artificial dissipation terms consist of combined second/fourth-order differences. The Beam-Warming algorithm uses second-order implicit artificial dissipation and requires the solution of a  $5 \times 5$  block tridiagonal system of equations. The diagonal algorithm uses an implicit dissipation that is identical to the explicit second/fourth-order dissipation, and requires the solution of scalar pentadiagonal equations. The diagonal algorithm requires fewer computational operations per time step than the Beam-Warming algorithm, and is therefore, more computationally efficient. However, Levy et al.<sup>26</sup> have shown that the diagonal algorithm has an inherent directional bias. If the angle of attack is too large, this may lead to a nonphysical vortex asymmetry in the flow. To avoid these complications, the computational results presented in this article and in Ref. 18 were computed using the Beam-Warming algorithm.

The numerical procedure advances the flow simulation in time by first updating the flow variables in Eq. (1) from time level  $n$  to  $n + 1$ . The time at  $n$  is given by  $t^n = n\Delta t$ , where the superscript  $n$  refers to the time level and  $\Delta t$  is the time step. Once the flow has been updated, a new roll angle is obtained from either Eq. (2) (forced-roll motions) or Eq. (4) (free-to-roll motions), and the grid rotated to the new roll angle. Equation (2) is algebraic and straightforward to evaluate. Equation (4) is an ordinary differential equation that is advanced in time according to the expression

$$\phi^{n+1} = (2\phi^n - \phi^{n-1}) + (\Delta t^2/I)[l^n - C_1 \text{sgn}(\nabla\phi^n)] \quad (5a)$$

where

$$\nabla\phi^n = \phi^n - \phi^{n-1} \quad (5b)$$

Equation (5b) is a first-order-accurate approximation to  $\dot{\phi}$ . Equation (5a) is second-order-accurate in time when  $\dot{\phi}$  does not change sign and is first-order-accurate otherwise.

The NSS code's spatial and time accuracy,<sup>17,18,25,27</sup> as well as a zonal grid capability for treating complex geometries,<sup>27</sup> has been previously demonstrated and reported in the literature.

#### Computational Grids

A three-dimensional hyperbolic grid generator<sup>28</sup> was used to generate a spherical-type grid for the 65-deg sweep delta wing in Fig. 3. All of the geometric features of the delta wing surface were modeled in the computational grid. However, the computational sting diameter was kept constant downwind of the wing trailing edge, whereas the experimental model had a reduced diameter. A perspective view of the wing surface grid and a portion of the sting are shown in Fig. 4. A portion of the viscous grid clustering normal to the wing at the trailing edge is also shown in this figure. The spherical axis extends upwind from the wing apex. The far-field boundaries are not shown in the figure, but extend two root-chord lengths upwind and downwind of the wing body, and five root-chord lengths in the body-normal direction. The grid consists of 67 points in the streamwise (longitudinal) direction,

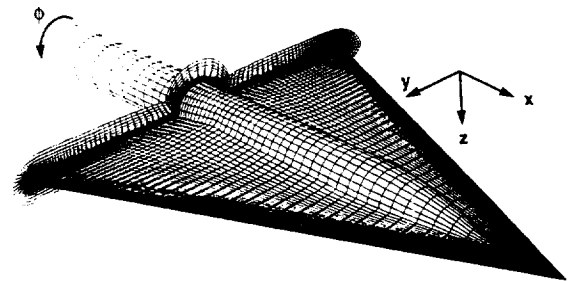


Fig. 4 Perspective view of the computational grid.

208 points in the circumferential direction, and 49 points in the body-normal direction, totaling about 700,000 grid points. There are more grid points on the leeward side of the wing (in the circumferential direction) than on the windward side to resolve the leeward side vortices. This grid is identical to the one used with the NSS code in Refs. 17 and 18 (see also Figs. 1 and 2).

The delta-wing grid was split into four zones in the streamwise direction. This was done in order to take full advantage of two available Cray C-90 supercomputers that had different amounts of main and secondary memories.

#### Numerical Boundary Conditions

The no-slip condition (zero velocity relative to a moving solid surface) is imposed on the wing and fuselage/sting surfaces, whereas density and pressure are found by extrapolation. The total energy per unit volume is then computed from the perfect gas law. Uniform flow is imposed at the far field, while a zero-gradient condition is used at the outflow boundary. Flow variables are averaged across the wake cut that extends from the wing trailing edge downwind to the outflow boundary. Boundary conditions are imposed on the spherical axis by averaging flow variables (one grid point off the axis) in the circumferential direction.

Zonal boundary conditions are updated sequentially with the most recent data available. Since the grids have coincident surfaces with identical grid points, data transfer from one grid to another is accomplished by direct injection. A more complete description of the zonal interface boundary conditions is given in Ref. 27.

#### Results

Three dynamic-roll cases were simulated, two forced-roll oscillations and one damped free-to-roll motion, using the time-dependent RANS equations. The direction of positive roll for the 65-deg sweep delta wing is shown in Fig. 4. This corresponds to the wing moving clockwise (right wing downward) as viewed from behind the wing facing forward (pilot view). In all cases, the freestream flow conditions were Mach number  $M_\infty = 0.27$ , angle of attack  $\alpha = 30$  deg, and Reynolds number based on the wing root chord  $Re_c = 3.67 \times 10^6$ .

Experimental data provided by Hanff and Huang<sup>10</sup> are used to validate the computed results. Experimental forces and moments for the forced-roll cases are obtained by taking an ensemble average over several cycles of motion and then using a fast Fourier transform to represent the forces and moments in terms of the first 10 harmonics of the motion. Thus, the time-history of the experimental forces and moments are a reconstruction of the Fourier decomposition. The computed time-history results also use an ensemble average over four cycles of motion. No attempt is made to decompose the computed results into Fourier components.

Each forced-roll case was started from a converged computation whose static roll angle corresponded to the maximum roll angle of the oscillation, i.e., where the dynamic-roll oscillation is momentarily at rest. This minimized the initial startup transients, which were found to completely decay during the first cycle of motion. Thus, the computations were found to be periodic during the second and following cycles.

#### Forced-Roll Oscillations

$\Phi_0 = 0$  Deg

The aerodynamic response for a 65-deg sweep delta wing undergoing a large-amplitude, high-rate roll motion about its longitudinal axis is obtained by numerically integrating the RANS equations with the NSS code subject to a forced rigid-body grid motion defined by Eq. (2). The first case has a zero offset angle ( $\Phi_0 = 0$  deg), a roll amplitude  $\Phi_{\max} = 28.2$  deg, and a frequency  $f = 10$  Hz. This frequency corresponds to a

reduced frequency [Eq. (3)] of  $k = 0.20$ . There are 15,000 time steps per cycle of motion. This corresponds to a non-dimensional time step  $\Delta\tau = 0.00362$  and a dimensional time step of  $\Delta t = 6.67 \times 10^{-6}$  s.

Figure 5 shows the leeward-side vortices for the delta wing at different instantaneous roll angles. The viewing angle is above the wing and perpendicular to the zero roll planform. This portion of the roll motion corresponds to the second half of a periodic cycle [Eq. (2)] where the right wing begins from rest at  $\phi = -28.2$  deg and moves in a clockwise direction (right wing downward) through zero roll and comes to rest again at  $\phi = 28.2$  deg. The maximum angular rate,  $\dot{\phi} = 1772$  deg/s, occurs at zero roll angle. The vortices are numerically visualized by computing instantaneous streamlines emanating from the delta-wing apex. These streamlines correspond to a flow that is considered frozen at an instant of time. The vortices visualized by this approach should realistically depict the vortex cores upwind of vortex breakdown, where transverse movement of the cores is slow. Instantaneous streamlines may be less realistic downwind of vortex breakdown, where the flow is highly nonsteady. The instantaneous location of the vortex breakdown positions and the corresponding direction of motion are indicated in the figure by arrows. Vortex breakdown is characterized by a rapid growth of the vortex core diameter and a rapid change in direction of the vortex core. Notice at  $\phi = -28.2$  deg (left wing down), vortex breakdown on the left wing occurs closer to the wing apex than does the right wing vortex breakdown location. As the wing rotates clockwise, the left wing breakdown position

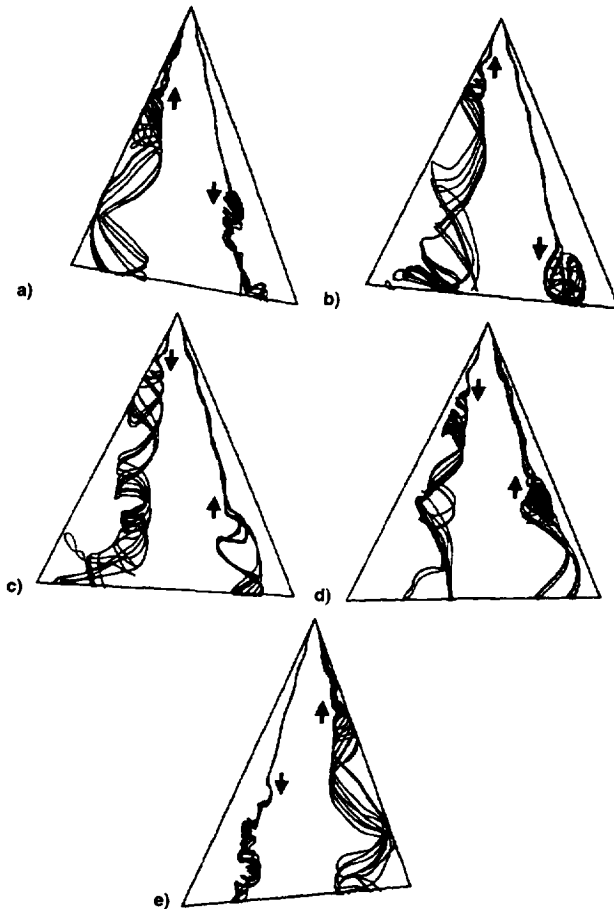


Fig. 5 Computed leeward-side vortices and vortex breakdown motions visualized by instantaneous streamlines for a forced-roll oscillation.  $M_\infty = 0.27$ ,  $\alpha = 30$  deg,  $\Phi_0 = 0$  deg,  $\Phi_{\max} = 28.2$  deg,  $k = 0.20$ , and  $Re = 3.67 \times 10^6$ .  $\phi =$  a)  $-28.2$ , b)  $-12.2$ , c)  $-2.2$ , d)  $12.6$ , and e)  $28.2$ .

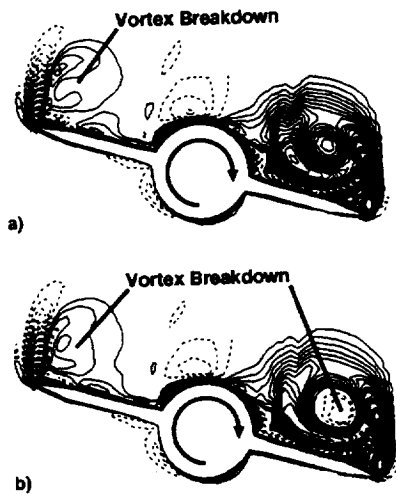


Fig. 6 Helicity-density visualization of crossflow vortices at  $\phi = 16.9$  deg,  $M_\infty = 0.27$ ,  $\alpha = 30$  deg,  $\Phi_0 = 0$  deg,  $\Phi_{\max} = 28.2$  deg,  $k = 0.20$ , and  $Re = 3.67 \times 10^6$ .  $x/c =$  a) 0.479 and b) 0.506.

first moves towards the wing apex, reverses direction near the apex, and then proceeds downwind towards the wing trailing edge. Conversely, the right wing breakdown position first moves downwind toward the wing trailing edge, reverses direction near the trailing edge, and then moves upwind towards the wing apex. The motion of vortex breakdown is therefore seen to traverse a large portion of the delta-wing length. There is a clear lag in the vortex breakdown motion relative to the forced-roll motion of the delta-wing body. As expected, the vortex breakdown positions on each side of the wing move in opposite directions relative to each other. Figures 5d and 5e show a large change in the instantaneous vortex breakdown positions, when the wing rolls from  $\phi = 12.6$  to  $28.2$  deg. This indicates the vortex breakdown positions move at a very high rate during this portion of the roll oscillation. The instantaneous streamlines in Fig. 5 imply spiral vortex breakdown. A separate nonsteady numerical flow visualization of the vortex core confirmed the presence of spiral vortex breakdown. This flow visualization was carried out in a postprocessing manner by releasing particles in the vortex core, near the delta-wing apex, and tracking their motion in time by integrating the nonsteady Navier-Stokes velocity field.

Figure 6 shows the instantaneous structure of the vortices in crossflow planes located just upwind and downwind of the right wing vortex breakdown, when the instantaneous roll angle is  $16.9$  deg and the wing is rotating clockwise. The streamwise location is approximately at 50% of the root chord. Helicity density<sup>29</sup> is used to visualize the vortices and is defined by

$$H_d = \mathbf{V} \cdot \boldsymbol{\Omega} \quad (6)$$

where  $\mathbf{V}$  is the fluid velocity and  $\boldsymbol{\Omega}$  is the fluid vorticity. A strong vortex will tend to have high-valued contours clustered about the vortex core, whereas a weaker vortex will tend to have low-valued contours sparsely spaced about the vortex core. The sign of helicity density indicates the direction of vortex rotation, when there is no vortex breakdown.<sup>29</sup> This allows the easy identification of primary, secondary, and tertiary structures. However, the helicity density of a vortex core can change sign when vortex breakdown occurs. This is due to the presence of local reversed flow. In Fig. 6, solid lines indicate positive helicity density, while dashed lines indicate negative helicity density. Primary, secondary, and tertiary vortices are present in the flow. In Fig. 6a there is vortex breakdown above the left wing while the right-wing vortex is still intact. In Fig. 6b, which is located slightly downwind of Fig. 6a, vortex breakdown occurs on both sides of the wing.

This is evident by the small pocket of reversed flow (dashed contours) in the right-wing vortex core. The sparseness of helicity-density contours at the right-wing vortex core also indicate its weakened state.

The computed and experimental<sup>10</sup> dynamic rolling-moment coefficients  $C_l$  are shown in Fig. 7. Computed static  $C_l$  values from Ref. 18 are also shown in Fig. 7, with additional static cases at  $\phi = \pm 65.6$  deg. Both the computed and experimental dynamic  $C_l$  are in good agreement with each other. Reducing the time step by a factor of 2 had no significant effect on the dynamic rolling-moment time history. Notice that the dynamic  $C_l$  is not simply a perturbation superimposed on the static  $C_l$  curve, as was the case in Fig. 1 where the flow had no vortex breakdown. The nonlinear time lags of the vortex breakdown position with respect to the delta-wing motion (see Fig. 5) are responsible for this marked difference. The area enclosed by a dynamic  $C_l$  curve indicates the amount of non-dimensional work done by the fluid on the wing. The computational and experimental nondimensional work are  $-3.4$  and  $-2.4$  deg, respectively. Moreover, both dynamic  $C_l$  curves trace out counterclockwise paths with increasing time, as indicated by the arrows in Fig. 7. The negative work and counterclockwise paths indicate the wing is positively damped under the present flow conditions. Since the work associated with the numerical flow is greater in magnitude than the work associated with the experimental flow, the computed flow is more highly damped than the experiment.

Figure 8 compares the computed and experimental dynamic normal-force coefficients,  $C_N$ . They are in fair agreement. Both curves have the same shape, but the computed normal loads are less than those found in the experiment. This is consistent with the static results shown in Ref. 18, where the computed suction peaks downwind of vortex breakdown were less than those found in experiment. Utilization of a finer grid in the crossflow direction should improve the comparison. The computed and experimental dynamic streamwise c.p. locations  $X_{c,p}$  are shown in Fig. 9. The agreement is good, with

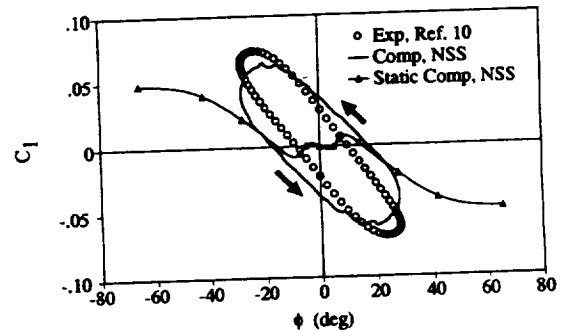


Fig. 7 Dynamic and static rolling-moment coefficients.  $M_\infty = 0.27$ ,  $\alpha = 30$  deg,  $\Phi_0 = 0$  deg,  $\Phi_{\max} = 28.2$  deg,  $k = 0.20$ , and  $Re = 3.67 \times 10^6$ .

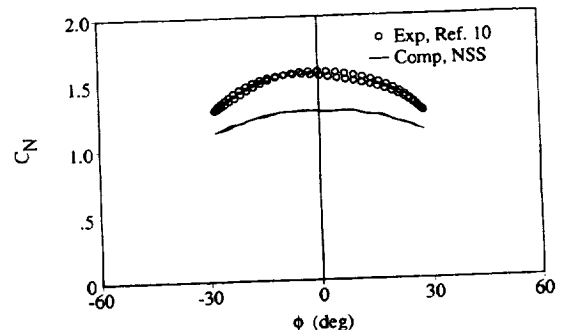


Fig. 8 Dynamic normal-force coefficients.  $M_\infty = 0.27$ ,  $\alpha = 30$  deg,  $\Phi_0 = 0$  deg,  $\Phi_{\max} = 28.2$  deg,  $k = 0.20$ , and  $Re = 3.67 \times 10^6$ .

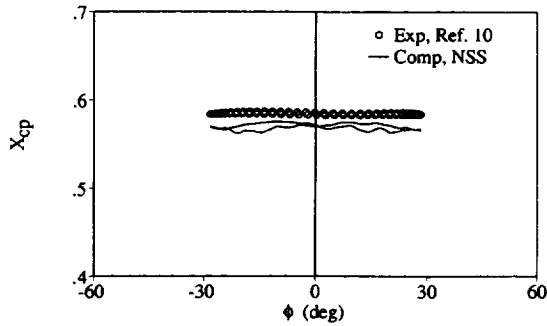


Fig. 9 Dynamic streamwise c.p. locations.  $M_\infty = 0.27$ ,  $\alpha = 30$  deg,  $\Phi_0 = 0$  deg,  $\Phi_{\max} = 28.2$  deg,  $k = 0.20$ , and  $Re = 3.67 \times 10^6$ .

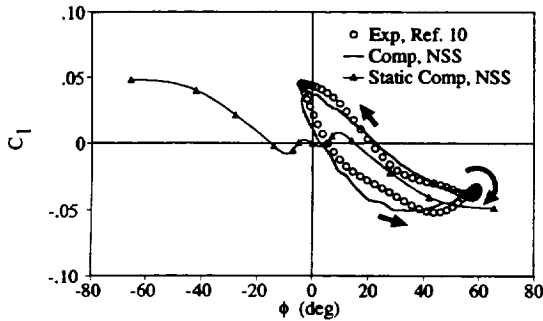


Fig. 10 Dynamic and static rolling-moment coefficients.  $M_\infty = 0.27$ ,  $\alpha = 30$  deg,  $\Phi_0 = 28.0$  deg,  $\Phi_{\max} = 31.9$  deg,  $k = 0.20$ , and  $Re = 3.67 \times 10^6$ .

the computed  $X_{c.p.}$  located slightly upwind of the experimentally measured values.

$\Phi_0 = 28$  Deg

A second forced dynamic-roll motion was computed with an offset angle  $\Phi_0 = 28.0$  deg, a roll amplitude  $\Phi_{\max} = 31.9$  deg, and  $f = 10$  Hz ( $k = 0.20$ ). This corresponds to a roll-angle range of  $-3.9 \leq \phi \leq 59.9$  deg. The nondimensional time step ( $\Delta\tau = 0.00362$ ) was identical to the previous case. The computed and experimental<sup>10</sup> dynamic  $C_l$  are shown in Fig. 10, together with computed static  $C_l$  values from Ref. 18. Arrows in the figure indicate how the experimental  $C_l$  vary with increasing time. Note that there is a large counterclockwise loop and a small clockwise loop. The counterclockwise loop corresponds to a damped portion of the wing motion, while the small clockwise loop ( $55.2 \leq \phi \leq 59.9$  deg) corresponds to an undamped portion of the wing motion. Good agreement is seen between the computed and experimental  $C_l$ . The dynamic  $C_l$  curves differ even more dramatically from the static curve than in the previous case. This behavior is again attributed to the large time lags in vortex breakdown motion. The nondimensional work done by the fluid on the wing is again evaluated by computing the net area enclosed by the dynamic curve, with the area inside the clockwise loop considered as positive. The computed and experimental net nondimensional work are  $-1.8$  and  $-1.4$  deg, respectively. These values, together with the dominant counterclockwise loop, indicate that this wing is also positively damped, as in the previous dynamic case. Moreover, the computed flow is again found to be more highly damped than the experiment.

The computed and experimental dynamic  $C_N$  are shown in Fig. 11 and are in good agreement with each other. Both curves form a figure-eight pattern. Note that the smaller  $C_N$  values in this dynamic case result in better agreement between computation and experiment than in the previous dynamic case, which had larger  $C_N$  values. This again suggests that further improvement could be obtained by refining the grid.

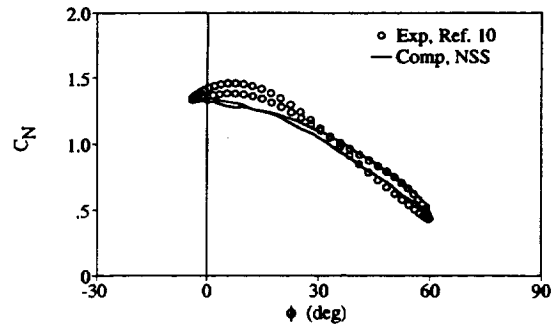


Fig. 11 Dynamic normal-force coefficients.  $M_\infty = 0.27$ ,  $\alpha = 30$  deg,  $\Phi_0 = 28.0$  deg,  $\Phi_{\max} = 31.9$  deg,  $k = 0.20$ , and  $Re = 3.67 \times 10^6$ .

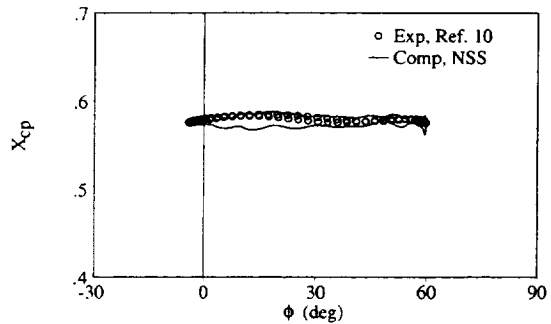


Fig. 12 Dynamic streamwise c.p. locations.  $M_\infty = 0.27$ ,  $\alpha = 30$  deg,  $\Phi_0 = 28.0$  deg,  $\Phi_{\max} = 31.9$  deg,  $k = 0.20$ , and  $Re = 3.67 \times 10^6$ .

Figure 12 shows the computed and experimental dynamic  $X_{c.p.}$ , which are in good agreement with each other.

#### Damped Free-to-Roll Motions

A final dynamic case is presented in which the delta wing is initially fixed at  $\phi = 40.5$  deg and then released. The wing is allowed to roll freely under the influence of the instantaneous aerodynamic rolling moment. The time-dependent RANS equations are therefore coupled with the flight dynamic equation of motion that has a single degree of freedom in roll, [see Eqs. (1) and (4)]. The details of this coupling were previously described in the Numerical Approach section. The nondimensional time step was  $\Delta\tau = 0.005$ .

Figure 13 shows the time-history of the computed and experimental<sup>6</sup> roll angles. Also shown in the figure is a roll simulation using a linearized model that was reported by Hanff.<sup>6</sup> The computed and experimental roll angles are in close agreement with each other for the first half-cycle of roll motion. Thereafter, the computed roll motion damps out more rapidly than the experiment. This result was anticipated, since both of the computational forced-roll motions described earlier exhibited greater damping than the experimental motions. The locations of the minimum and maximum peaks in the computed roll-angle oscillations are nearly identical to those found in the experiment. This indicates the computed frequency of motion is close to the experimental frequency. On the other hand, the linearized simulation of Hanff<sup>6</sup> has a lower frequency and takes much longer to damp out. The final computed and experimental roll angles, where the delta wing comes to rest, were  $17.5$  and  $20.3$  deg, respectively. The computational static  $C_l$  curve in Fig. 2 has a zero rolling moment at  $\phi \approx 16$  deg. The difference between this static roll angle trim point and the final static roll angle in the damped free-to-roll computation is due to the friction term in Eq. (4).

The phase-plane curve  $\dot{\phi}(t)$  vs  $\phi$ , is shown in Fig. 14. This trajectory begins at  $\phi = 40.5$  deg and  $\dot{\phi} = 0$ . The curve follows a clockwise path until it reaches the final static condition at  $\phi = 17.5$  deg. The final roll angle for the free-to-roll experiment is also shown in the figure.

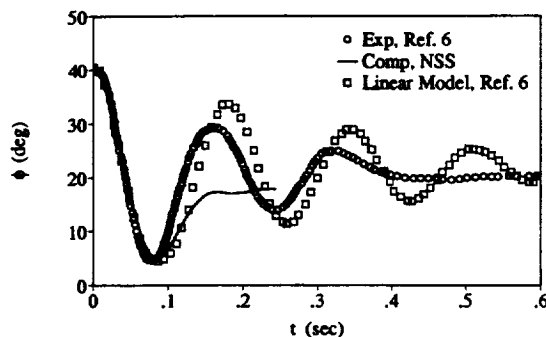


Fig. 13 Time history of roll angle for free-to-roll motion.  $M_\infty = 0.27$ ,  $\alpha = 30$  deg,  $\Phi_0 = 40.5$  deg, and  $Re = 3.67 \times 10^6$ .

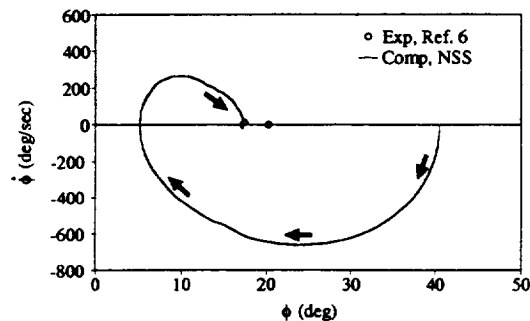


Fig. 14 Phase-plane path for a damped free-to-roll motion.  $M_\infty = 0.27$ ,  $\alpha = 30$  deg,  $\Phi_0 = 40.5$  deg, and  $Re = 3.67 \times 10^6$ .

### Conclusions

The dynamic flowfield about a 65-deg sweep delta wing at 30-deg angle of attack and  $Re = 3.67 \times 10^6$  was numerically simulated using the time-dependent, three-dimensional, RANS equations. Two large-amplitude, high-rate, forced-roll motions, and a damped free-to-roll motion were investigated. The latter computation coupled the RANS equations to the flight dynamic equation of motion with a single degree of freedom in roll. Vortex breakdown was present in each case.

The forced-roll computations were validated by comparing the computed and experimental normal-force coefficients, rolling-moment coefficients, and streamwise c.p. locations. The overall agreement was good, with some differences attributed to grid coarseness. There were large time lags in the vortex breakdown motion relative to the forced-roll motion of the delta-wing body. This resulted in a complex hysteresis of the dynamic rolling moment coefficient that differed substantially from previously published static results. The wing motion was positively damped in both cases.

A free-to-roll motion was also computed, where the delta wing was initially released from rest at 40.5 deg of roll. The resulting computational free-to-roll motion damped out more rapidly than the experiment, but the computed and experimental frequencies were in good agreement. There were three possible statically stable trim points. The computed and experimental roll motions went to the same trim point.

### Acknowledgments

The authors would like to thank E. S. Hanff and X. Z. Huang of the Canadian Institute of Aerospace Research for their helpful discussions and for providing the experimental data.

### References

- <sup>1</sup>Nguyen, L. T., Yip, L., and Chambers, J. R., "Self-Induced Wing Rock of Slender Delta Wings," AIAA Paper 81-1983, Aug. 1981.
- <sup>2</sup>Levin, D., and Katz, J., "Dynamic Load Measurements with Delta Wings Undergoing Self-Induced Roll Oscillations," *Journal of Aircraft*, Vol. 21, No. 1, 1984, pp. 30-36.
- <sup>3</sup>Arena, A. S., Jr., and Nelson, R. C., "The Effect of Asymmetric Vortex Wake Characteristics on a Slender Delta Wing Undergoing Wing Rock Motion," AIAA Paper 89-3348, Aug. 1989.
- <sup>4</sup>Arena, A. S., Jr., and Nelson, R. C., "An Experimental Study of the Nonlinear Dynamic Phenomenon Known as Wing Rock," AIAA Paper 90-2812, Aug. 1990.
- <sup>5</sup>Morris, S. L., and Ward, D. T., "A Video-Based Experimental Investigation of Wing Rock," AIAA Paper 89-3349, Aug. 1989.
- <sup>6</sup>Hanff, E. S., and Jenkins, S. B., "Large-Amplitude High-Rate Roll Experiments on a Delta and Double Delta Wing," AIAA Paper 90-0224, Jan. 1990.
- <sup>7</sup>Hanff, E. S., Kapoor, K., Anstey, C. R., and Prini, A., "Large-Amplitude High-Rate Roll Oscillation System for the Measurement of Non-Linear Airloads," AIAA Paper 90-1426, June 1990.
- <sup>8</sup>Hanff, E. S., and Huang, X. Z., "Roll-Induced Cross-Loads on a Delta Wing at High Incidence," AIAA Paper 91-3223, Sept. 1991.
- <sup>9</sup>Huang, X. Z., and Hanff, E. S., "Prediction of Leading-Edge Vortex Breakdown on a Delta Wing Oscillating in Roll," AIAA Paper 92-2677, June 1992.
- <sup>10</sup>Hanff, E. S., and Huang, X. Z., private communication, Inst. for Aerospace Research, Ottawa, ON, Canada, 1992-1994.
- <sup>11</sup>Jenkins, J. E., Myatt, J. H., and Hanff, E. S., "Body-Axis Rolling Motion Critical States of a 65-Degree Delta Wing," AIAA Paper 93-0621, Jan. 1993.
- <sup>12</sup>Arena, A. S., Jr., and Nelson, R. C., "Unsteady Surface Pressure Measurements on a Slender Delta Wing Undergoing Limit Cycle Wing Rock," AIAA Paper 91-0434, Jan. 1991.
- <sup>13</sup>Lee, E. M., and Batina, J. T., "Conical Euler Methodology for Unsteady Vortical Flows About Rolling Delta Wings," AIAA Paper 91-0730, Jan. 1991.
- <sup>14</sup>Kandil, O. A., and Salman, A. A., "Effects of Leading-Edge Flap Oscillation on Unsteady Delta Wing Flow and Rock Control," AIAA Paper 91-1796, June 1991.
- <sup>15</sup>Lee-Rausch, E. M., and Batina, J. T., "Conical Euler Analysis and Active Roll Suppression for Unsteady Vortical Flows About Rolling Delta Wings," NASA TP-3259, March 1993.
- <sup>16</sup>Kandil, O. A., and Salman, A. A., "Three-Dimensional Simulation of Slender Delta Wing Rock and Divergence," AIAA Paper 92-0280, Jan. 1992.
- <sup>17</sup>Chaderjian, N. M., "Navier-Stokes Prediction of Large-Amplitude Delta-Wing Roll Oscillations," *Journal of Aircraft*, Vol. 31, No. 6, 1994, pp. 1333-1340.
- <sup>18</sup>Chaderjian, N. M., and Schiff, L. B., "Navier-Stokes Prediction of a Delta Wing in Roll with Vortex Breakdown," AIAA Paper 93-3495, Aug. 1993.
- <sup>19</sup>Pulliam, T. H., and Steger, J. L., "Implicit Finite Difference Simulations of Three-Dimensional Compressible Flow," *AIAA Journal*, Vol. 18, No. 2, 1980, pp. 159-167.
- <sup>20</sup>Baldwin, B. S., and Lomax, H., "Thin Layer Approximation and Algebraic Model for Separated Turbulent Flow," AIAA Paper 78-257, Jan. 1978.
- <sup>21</sup>Degani, D., and Schiff, L. B., "Computation of Supersonic Viscous Flows Around Pointed Bodies at Large Incidence," AIAA Paper 83-0034, Jan. 1983.
- <sup>22</sup>Degani, D., and Schiff, L. B., "Computation of Turbulent Supersonic Flows Around Pointed Bodies Having Crossflow Separation," *Journal of Computational Physics*, Vol. 66, No. 1, 1986, pp. 173-196.
- <sup>23</sup>Beam, R. M., and Warming, R. F., "An Implicit Finite-Difference Algorithm for Hyperbolic Systems in Conservation Law Form," *Journal of Computational Physics*, Vol. 22, No. 1, 1976, pp. 87-110.
- <sup>24</sup>Pulliam, T. H., and Chaussee, D. S., "A Diagonal Form of an Implicit Approximate-Factorization Algorithm," *Journal of Computational Physics*, Vol. 39, No. 2, 1981, pp. 347-363.
- <sup>25</sup>Chaderjian, N. M., "Comparison of Two Navier-Stokes Codes for Simulating High-Incidence Vortical Flow," *Journal of Aircraft*, Vol. 30, No. 3, 1993, pp. 357-364.
- <sup>26</sup>Levy, Y., Hesselink, L., and Degani, D., "Anomalous Asymmetries in Flows Generated by Algorithms that Fail to Conserve Symmetry," AIAA Paper 94-2287, June 1994.
- <sup>27</sup>Flores, J., and Chaderjian, N. M., "Zonal Navier-Stokes Methodology for Flow Simulation About a Complete Aircraft," *Journal of Aircraft*, Vol. 27, No. 7, 1990, pp. 583-590.
- <sup>28</sup>Steger, J. L., and Rizk, Y. M., "Generation of Three Dimensional Body Fitted Coordinates Using Hyperbolic Partial Differential Equations," NASA TM 86753, June 1985.
- <sup>29</sup>Levy, Y., Degani, D., and Seginer, A., "Graphical Visualization of Three-Dimensional Vortical Flows by Means of Helicity," *AIAA Journal*, Vol. 28, No. 8, 1990, pp. 1347-1352.